Supporting Information

IrO$_2$-stablized La$_2$IrO$_6$ perovskite nanotubes via corner-shared interconnections as highly-efficient oxygen evolution electrocatalysts

Yuwei Jin, Wenjing Huo, Libin Zhang, Yong Li, Shuo Yang, Jinjie Qian, Dong Cai,

*Yongjie Ge, Xuemei Zhou *, Zhi Yang*, Huagui Nie, **

Y. W. Jin, W. J. Huo, Dr. D. Cai, Dr. Y. J. Ge, Dr. X. M. Zhou, Prof. J. J. Qian, Prof. Z. Yang, Prof. H. G. Nie

Key Laboratory of Carbon Materials of Zhejiang Province, Wenzhou University, Wenzhou 325035, China

E-mail: zxm.mei@163.com; yang201079@126.com; huaguinie@126.com

Dr. S. Yang
College of Electrical and Electronic Engineering, Wenzhou University, Wenzhou 325035, China

Dr. L. B. Zhang
Hangzhou Electric Connector Factory, Hangzhou, 310052, China.

Prof. Y. Li
College of Mechanical and Electrical Engineering, Wenzhou University, Wenzhou, 325035, China

Methods

Chemicals and reagents: Lanthanum nitrate hexahydrate (La $(NO_3)_3 \cdot 6H_2O$, 99.99%), and polyvlnylpyrrolidone $(C_6H_9NO)_n$, MW=1300000) were purchased from Aladdin. Potassium hexachloroindate (K_2IrCl_6, 99.99%) and N, N-Dimethylformamide (C_3H_7NO, 99%) were purchased from Macklin. All the chemicals and reagents were without further purification.

Synthesis of La$_2$IrO$_6$/IrO$_2$ hollow nanotubes: In a typical synthesis process, 216.5 mg La($NO_3)_3 \cdot 6H_2O$ and 241.5 mg K_2IrCl_6 (the molar ratio was 1:1) were dissolved in a mixed solution of 2 mL ethanol and 8 mL N, N-Dimethylformamide. PVP (15% wt.) was dissolved in the prepared precursor solution to increase the viscosity for electrospinning. The final spinning solution was then transferred into a syringe and clamped into a syringe pump. Electrospinning was performed in MSK-NFES-1. The applied electrical potential to the tip was 20 kV, and the distance from the needle tip (fed at a rate of 0.6 mL h^{-1}) to the collector was 15 cm. Samples were collected on silicone oil paper. The temperature of the whole system is kept at 40°C. The as-prepared membrane was then calcined in air at 750°C (the heating rate was 0.5°C min^{-1}) and the nanofiber precursor was obtained. Then the La$_2$IrO$_6$/IrO$_2$ nanotubes were obtained by the treatment of HCL. As a contrast, the IrO$_2$ nanowires were prepared under the same conditions without addition of La($NO_3)_3 \cdot 6H_2O$.

Characterizations: X-ray diffraction patterns (XRD) were acquired with a D/MAX-2400 diffractometer using Cu Kα radiation (40 kV, 100 mA, λ = 1.54056 Å). Scanning electron microscopy (SEM) images were obtained from a JSM-6700 (spot 3.0, 15 kV). Transmission electron microscopy (TEM), high resolution TEM (HRTEM), and energy dispersive X-ray spectroscopy (EDS) elemental mapping were performed with a JEOL-2100F instrument (200 kV). X-ray photoelectron spectroscopy (XPS) measurements were executed with an ultrahigh-vacuum setup, equipped with a monochromatic Al Ka X-ray source (10 mA, 15 kV) and a high resolution Gammadata-Scienta SES 2002 analyzer. The Raman spectra were recorded on a Renishaw in Via Raman microscope using a 785 nm line of an Ar-ion laser.

Electrochemical measurement: All electrochemical measurements were performed in

0.5 M H_2SO_4 with a three-electrode system by using a CHI760E electrochemical workstation (CH Instrument Inc.) at room temperature. A Pt net and a saturated calomel (SCE) electrode were used as the counter electrode and the reference electrode, respectively. In our work, The SCE was calibrated by the reversible hydrogen electrode (RHE) through the equation $E_{vs.RHE} = E_{vs.SCE} + 0.264\,V$.[1-3]

For the preparation of the working electrodes, the powdered catalyst (4 mg) was dispersed in deionized H_2O (1 mL) and 10 μL of the resulting mixture was then drop-casted onto a carbon fiber paper. Nafion solution (5 μL, 0.2 wt.% in ethyl alcohol) was then drop past on the dried ink. The working electrode had a catalyst loading of ca. 0.56 mg cm^{-2}.

Linear sweep voltammetry (LSV) was performed at a scan rate of 10 mV s^{-1}. The data in this work were compensated by 90% iR-drop. To estimate the double-layer capacitance, cyclic voltammetry (CV) was performed in the potential range from 0.3 to 0.4 V with various scan rates (10, 20, 30, 40 and 50 mV s^{-1}). For assessment of the OER activities, Tafel plots were obtained from LSV curves. According to the Tafel equation: $\eta = b\,log\,j + a$, the Tafel slope (b) can be obtained by fitting the linear portion of the Tafel plots.[4, 5] Electrochemical impedance spectroscopy (EIS) measurements were carried out over the frequency range from 100 kHz to 0.01 Hz at the potential of 1.3 V with an amplitude potential of 5 mV. Multi-Current Steps (ISTEP) was used to estimate stability with continuously constant current densities (10 mA cm^{-2}).

Computational methods：

All the calculations were performed within the framework of the density functional theory (DFT) as implemented in the Vienna Ab initio Software Package (VASP 5.4.4) code within the Perdew–Burke–Ernzerhof (PBE) generalized gradient approximation and the projected augmented wave (PAW) method[6-8]. The cutoff energy for the plane-wave basis set was set to 400 eV. The Brillouin zone of the surface unit cell was sampled by Monkhorst–Pack (MP) grids for IrO_2 and La_2IrO_6/IrO_2 structure optimizations[9]. The IrO_2 and La_2IrO_6/IrO_2 surfaces were determined by $2 \times 2 \times 1$ Monkhorst−Pack grid. The convergence criterion for the electronic self-consistent iteration and force was set to 10^{-5} eV and 0.01 eV/Å, respectively. A vacuum layer of

15 Å was introduced to avoid interactions between periodic images.

The free energies of adsorbates and transition states at temperature T were estimated according to the harmonic approximation, and the entropy is evaluated using the following equation:

$$S(T) = k_B \sum_i^{harm\,DOF} \left[\frac{\varepsilon_i}{k_B T \left(e^{\varepsilon_i/k_B} - 1 \right)} - \ln \left(1 - e^{-\varepsilon_i/k_B T} \right) \right]$$

where k_B is Boltzmann's constant and DOF is the number of harmonic energies (ε_i) used in the summation denoted as the degree of freedom, which is generally 3N, where N is the number of atoms in the adsorbates or transition states. Meanwhile, the free energies of gas phase species are corrected as:

$$G_g(T) = E_{elec} + E_{ZPE} + \int C_p \, dT - TS(T)$$

where C_p is the gas phase heat capacity as a function of temperature derived from Shomate equations and the corresponding parameters in the equations were obtained from NIST.
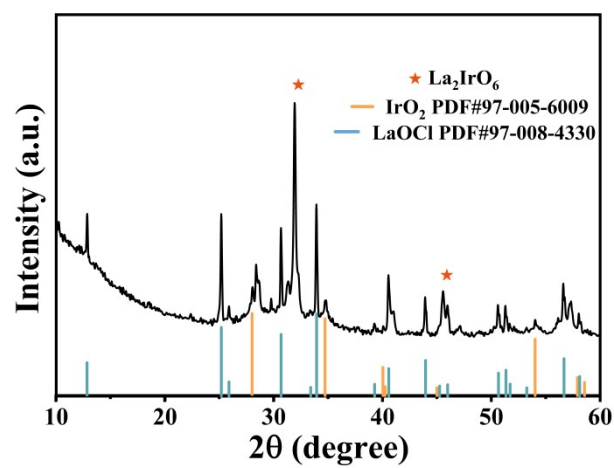
Fig. S1. XRD patterns for samples without acid treatment.
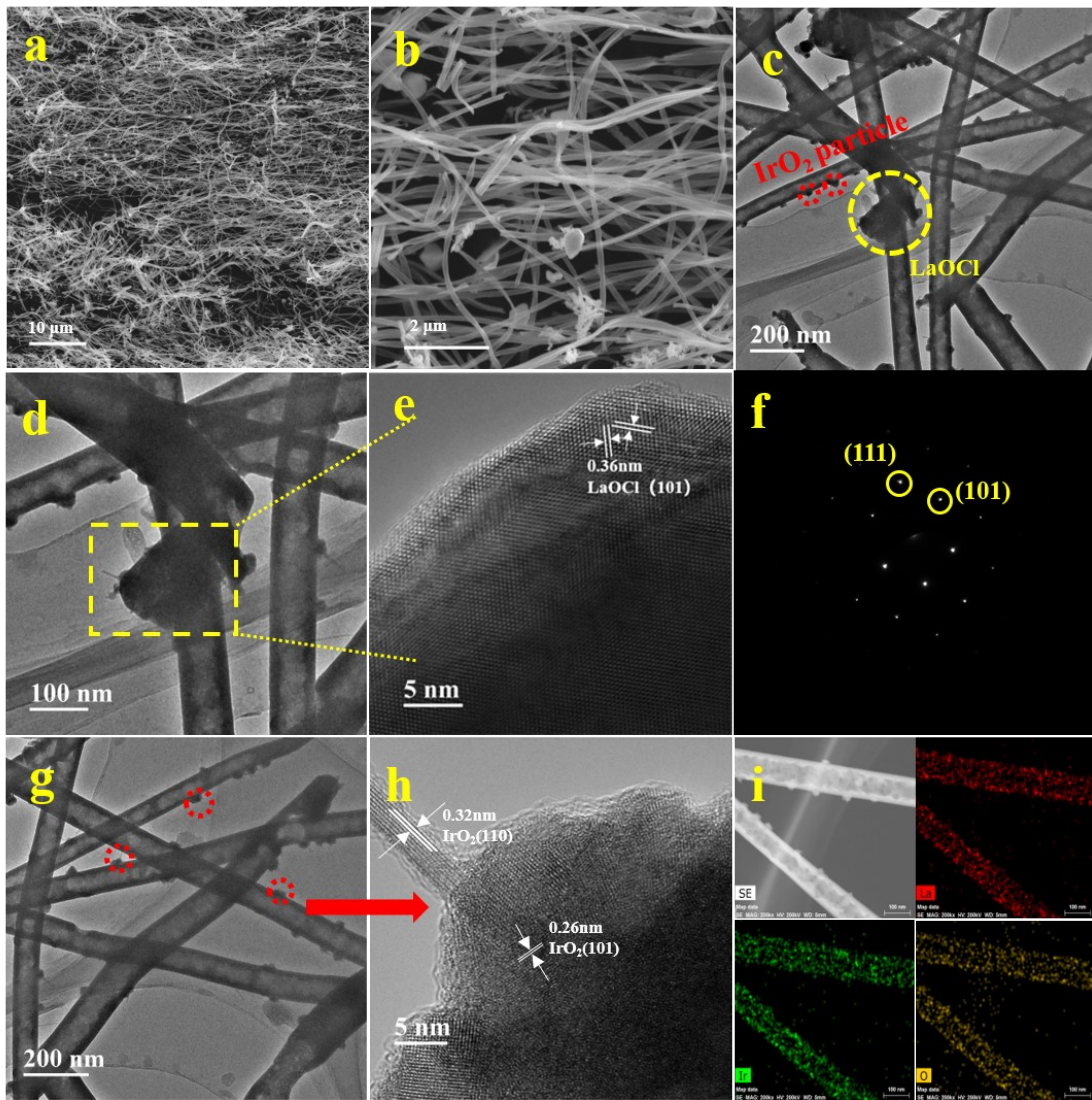
Fig. S2. SEM (a, b) and TEM (c) images for samples without acid treatment; enlarged TEM (d) and HRTEM (e) images and selected area electron diffraction (f) for LaOCl; enlarged TEM (g) and HRTEM (h) and the corresponding STEM elemental mapping (i) images for IrO_2.
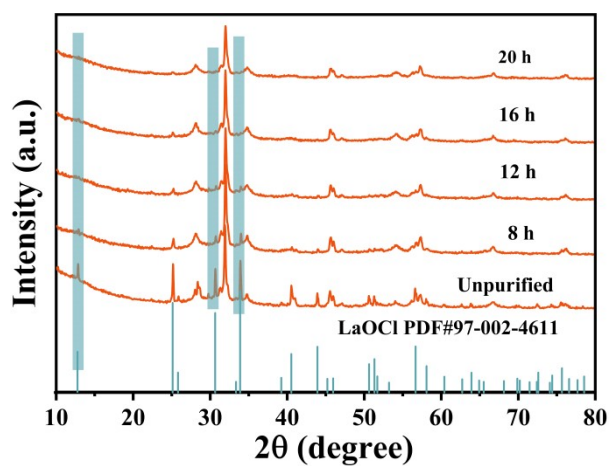
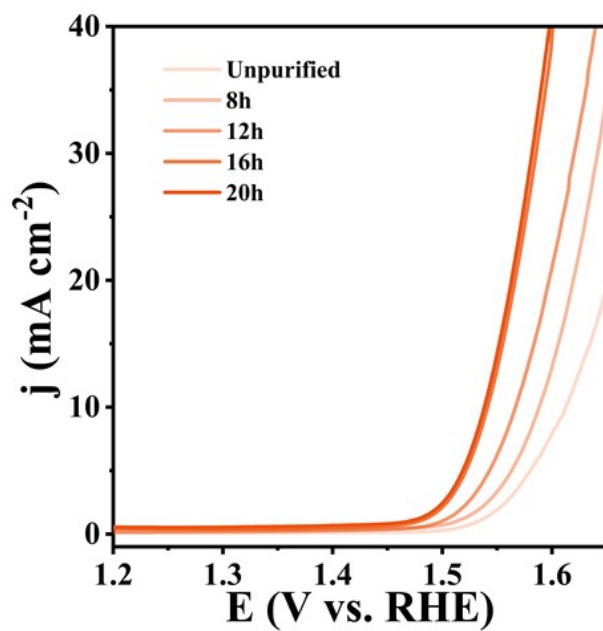**Fig. S3.** XRD patterns for samples with HCl treatment via different time.

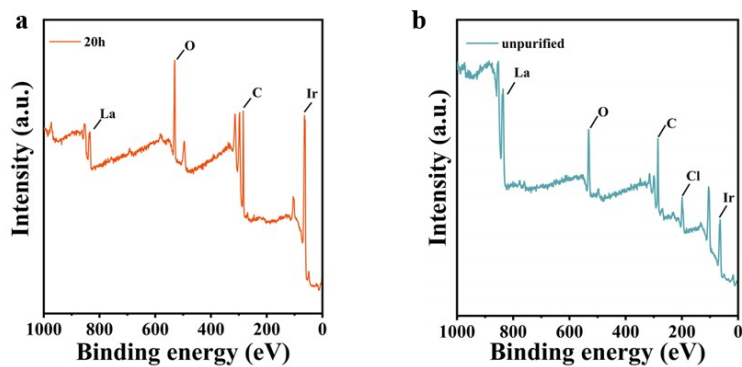**Fig. S4.** LSV curves for the samples with different HCl treatment time in 0.5 M H_2SO_4.

Fig. S5. XPS spectrum for samples with HCl treatment (a) and without acid treatment samples (b).
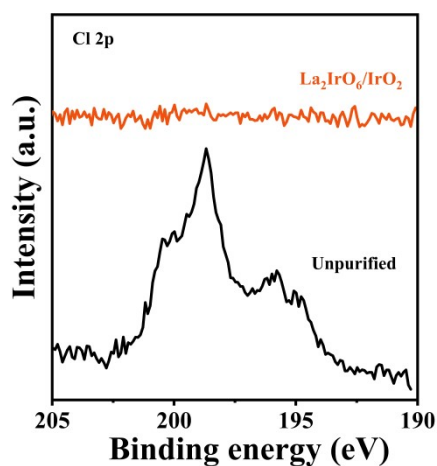
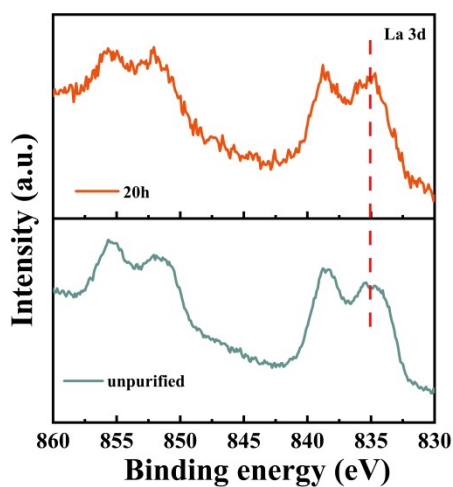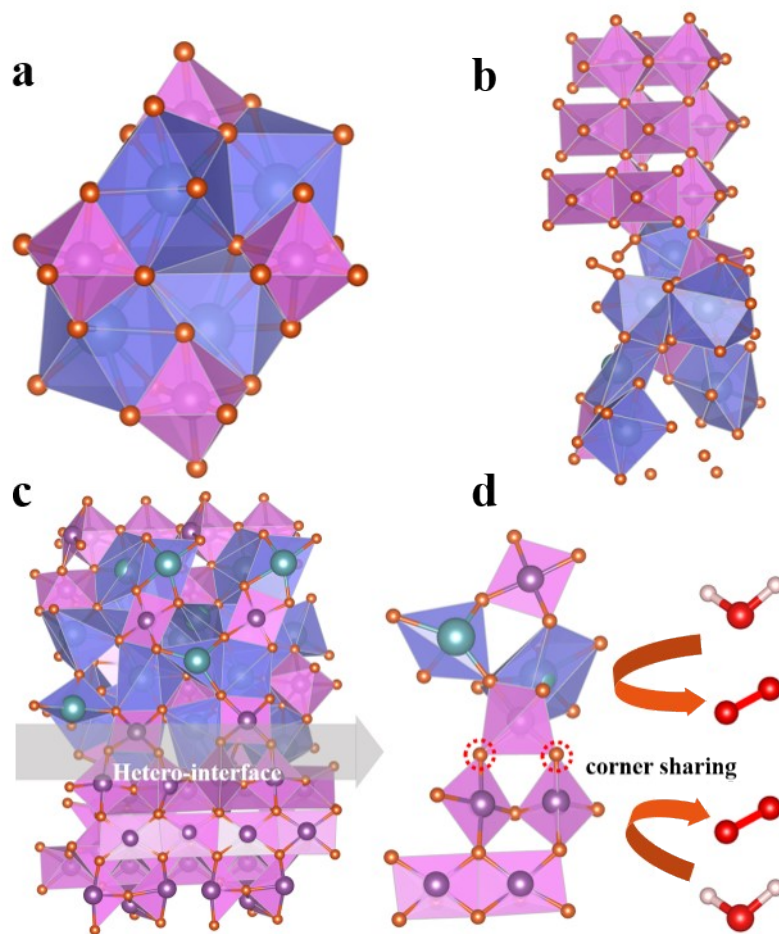**Fig. S6.** high-resolution XPS spectrum of Cl 2p for La_2IrO_6/IrO_2 and without acid treatment samples.

Fig. S7. The high-resolution XPS spectrum of La 3d for La_2IrO_6/IrO_2 and without acid treatment samples.

Fig. S8： The structure of La_2IrO_6 (a) and La_2IrO_6/IrO_2 with face-sharing IrO_6 (b) and corner-sharing IrO_6 (c, d) obtained by DFT.

Table S1: Structural parameters measured and obtained by DFT.

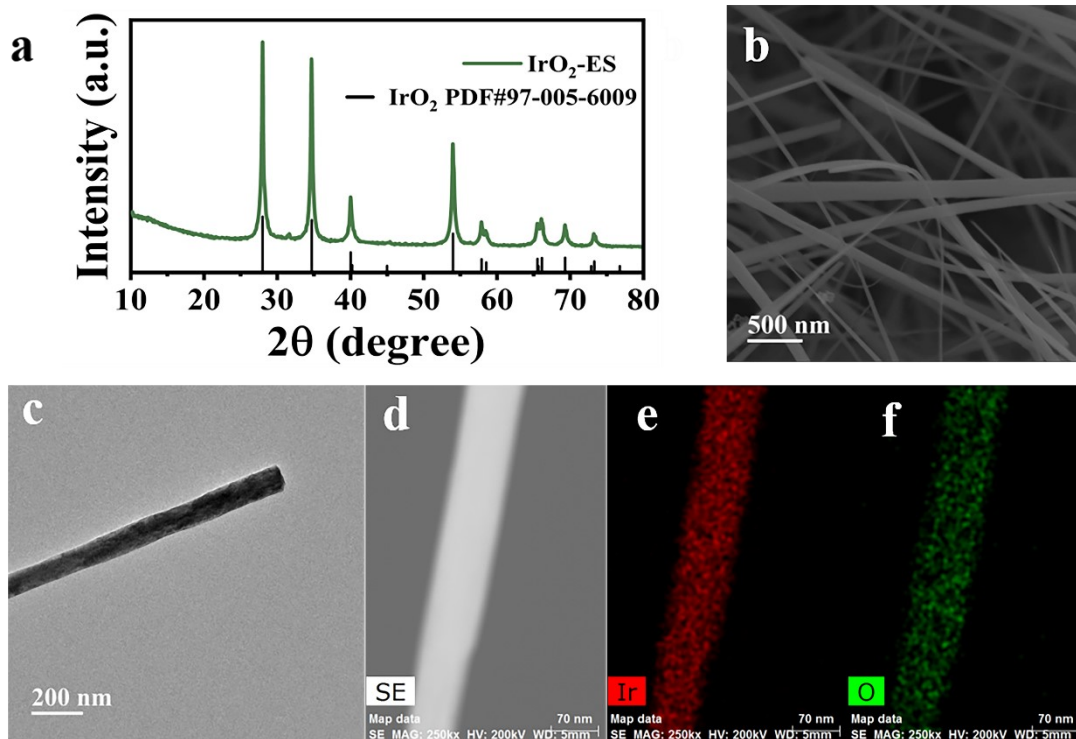|	La_2IrO_6	La_2IrO_6/IrO_2 (corner-sharing IrO_6)	La_2IrO_6/IrO_2 (face-sharing IrO_6)
a (Å)	5.51110	21.55880	6.40866
b (Å)	5.89495	13.12580	6.24187
c (Å)	7.76775	20.82680	20.91172
β (°)	91.8627	90.0000	90.0000
Formation energy (eV)	-5.41449	-5.871183	-5.715945

Fig. S9. (a) XRD patterns for IrO$_2$-ES; SEM (b), TEM (c) and the corresponding STEM elemental mappings images (d-f).
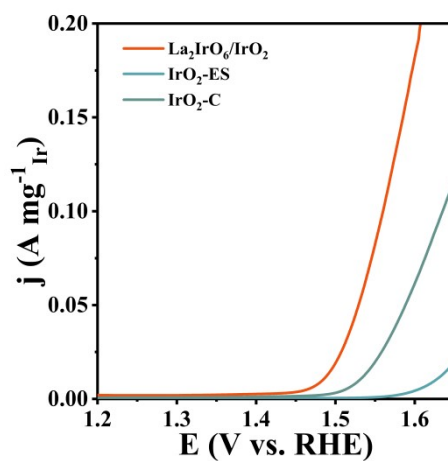

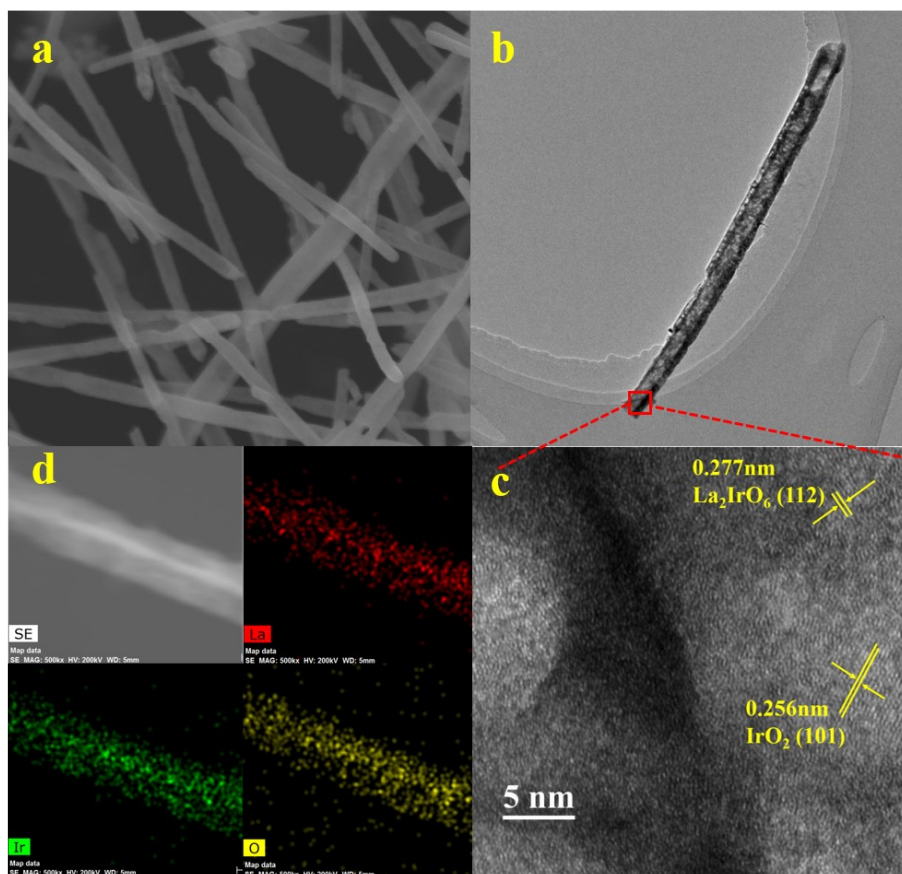**Fig. S10**. LSV for different electrodes based on mass activity.

Fig. S11. SEM (a), TEM (b), HRTEM (c) and (d) the corresponding STEM elemental mappings images of La_2IrO_6/IrO_2 after the stability test.
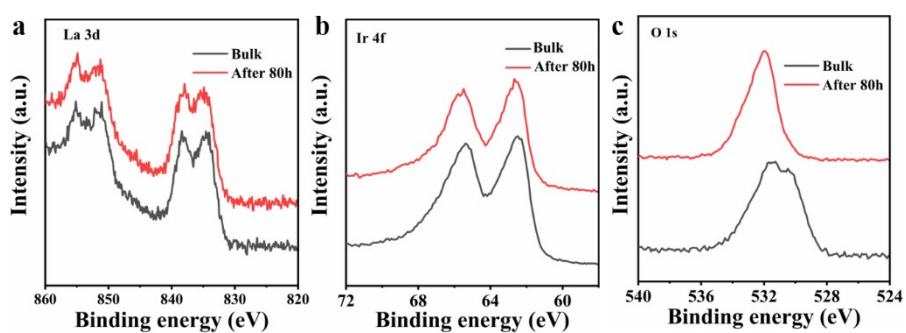

Fig. S12 The high-resolution XPS spectrum of Ir 4f (a), La 3d (b) and O 2p (c) for La_2IrO_6/IrO_2 after the stability test.
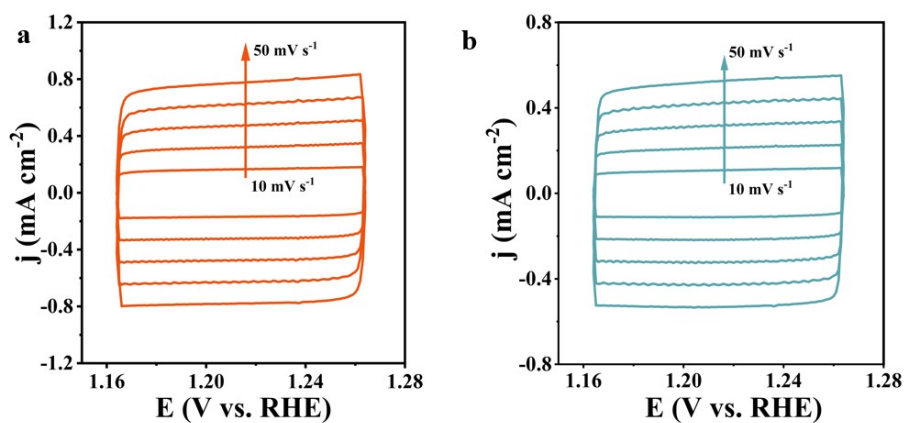
Fig. S13. Cyclic voltammograms for La_2IrO_6/IrO_2 (a) and IrO_2-ES (b) in the non-faradaic capacitance current range at scan rates of 10, 20, 30, 40 and 50 mV s^{-1}.

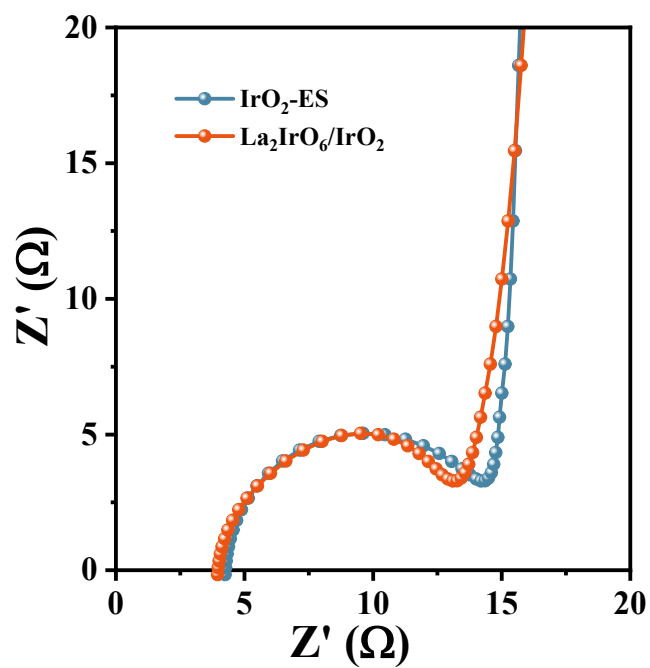**Fig. S14**. EIS spectra for La_2IrO_6/IrO_2 and IrO_2-ES.
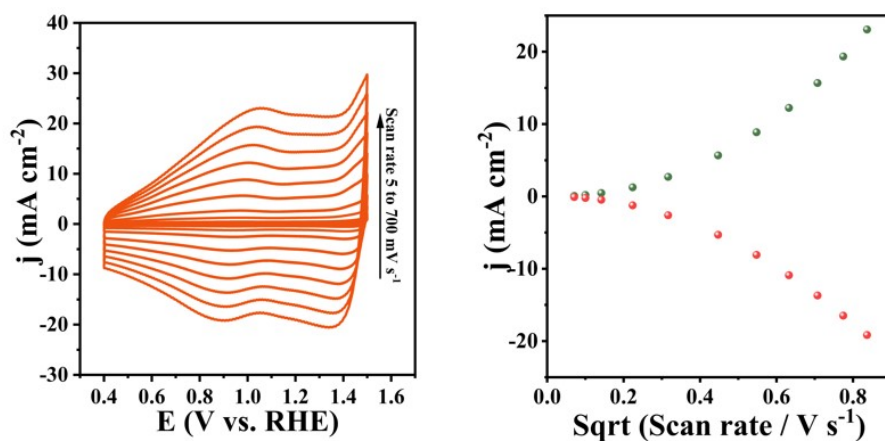
Fig. S15 Analysis of La$_2$IrO$_6$/IrO$_2$ by Laviron equation. CVs of La$_2$IrO$_6$/IrO$_2$ with scan rates from 5 to 700 mV s^{-1}. The plot of the redox peak currents densities versus the square root of scan rates of La$_2$IrO$_6$/IrO$_2$.

Fig. S16 Analysis of IrO$_2$-ES by Laviron equation. CVs of IrO$_2$-ES with scan rates from 5 to 700 mV s^{-1}. The plot of the redox peak currents densities versus the square root of scan rates of IrO$_2$-ES.
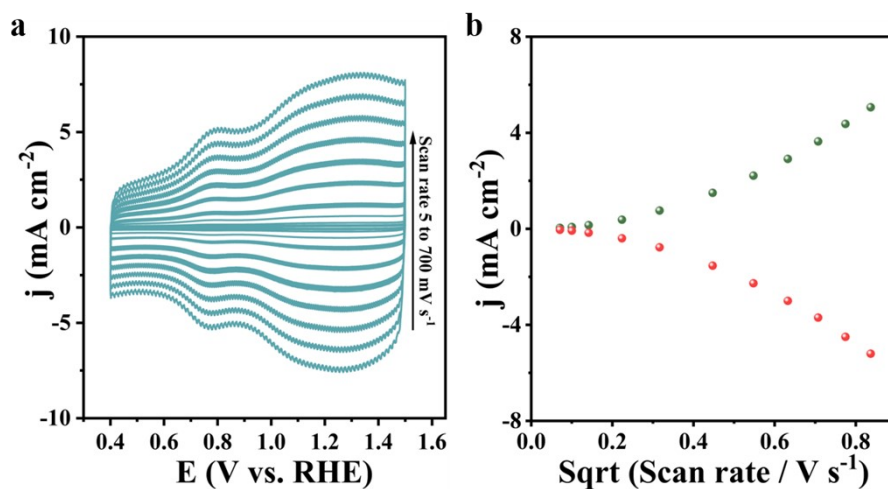
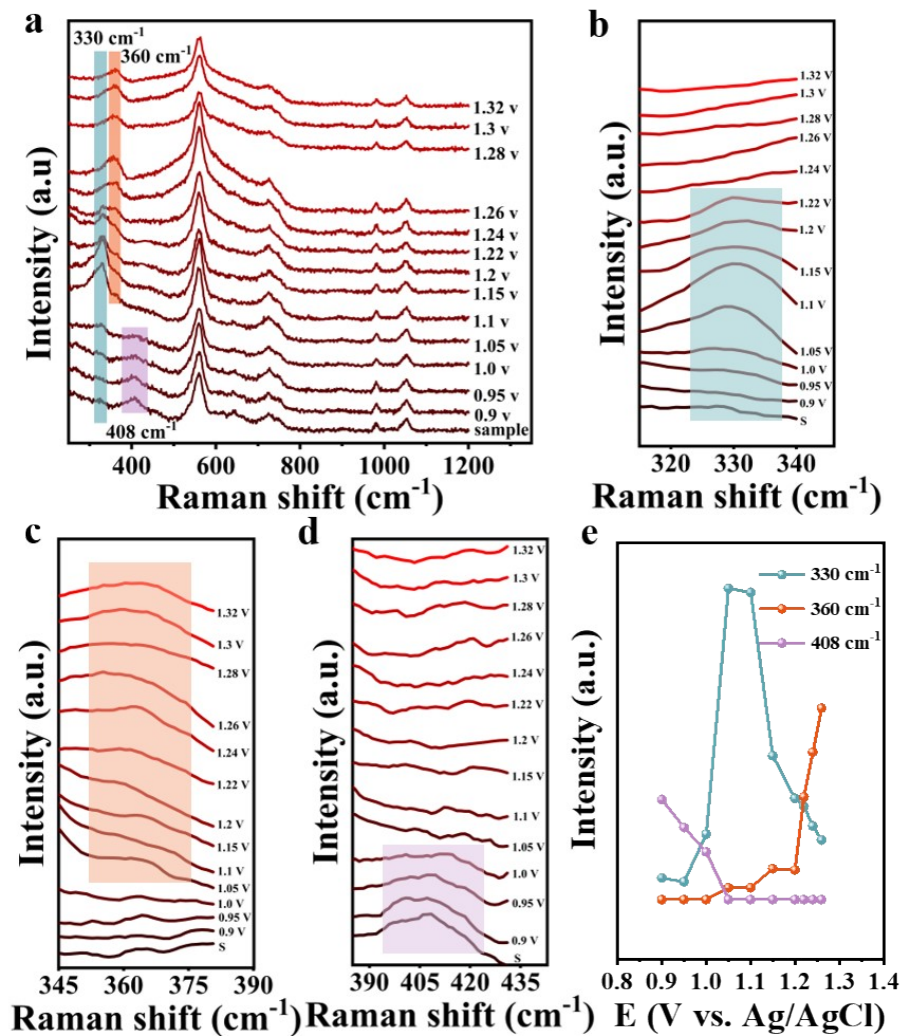**Fig. S17** In situ Raman spectra of La$_2$IrO$_6$/IrO$_2$ (a), enlargement of Raman spectra (b-d), (e) the intensity of Raman peaks obtained from **Fig. S16a** labeled under different potential.
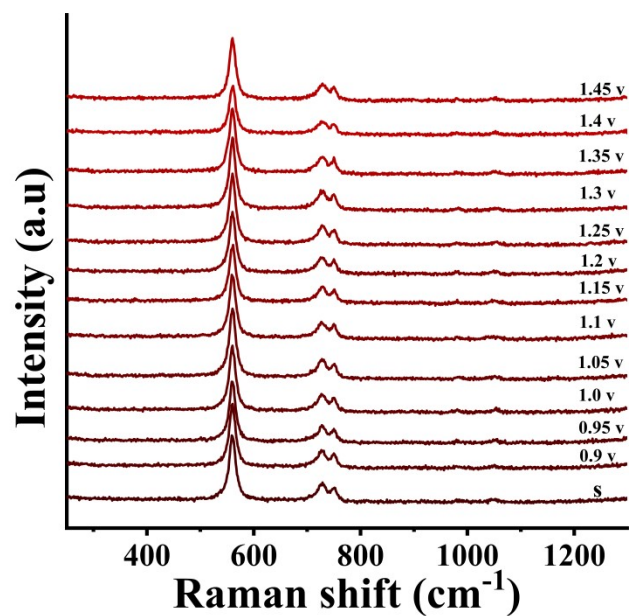
Fig. S18 In situ Raman spectra of IrO_2.
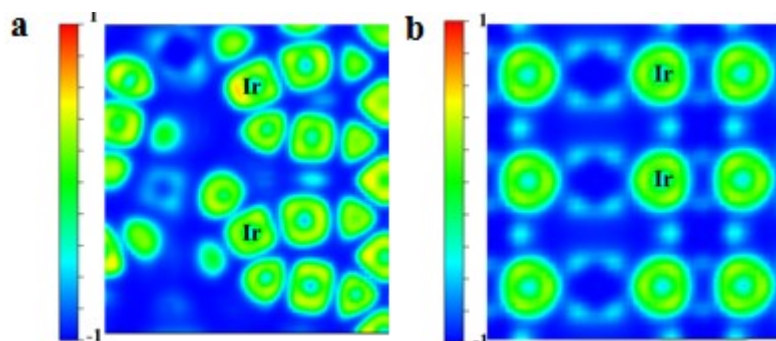
Fig. S19 ELF distribution of the La_2IrO_6/IrO_2 (a) and pure IrO_2 (b), and blue to red indicated a gradual increase in charge localization.
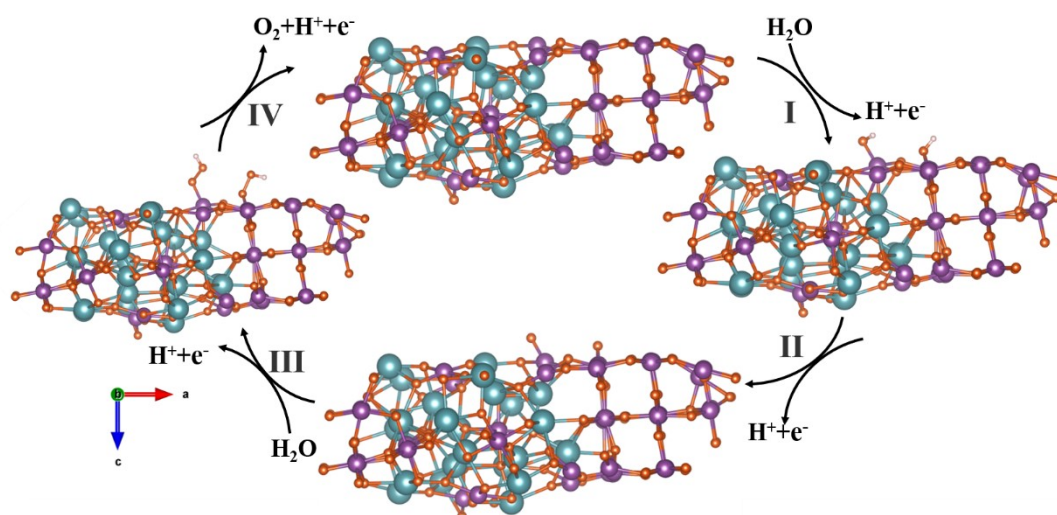
Fig. S20 The four electron OER pathway of Ir in both components in La_2IrO_6/IrO_2 as the active sites.

Fig. S21. The four electron OER pathway of single-component La_2IrO_6 in La_2IrO_6/IrO_2 as the active sites.

Fig. S22. The four electron OER pathway of single-component IrO_2 in La_2IrO_6/IrO_2 as the active sites.

Fig. S23. The four electron OER pathway of IrO_2.

Fig. S24. The overpotential versus different catalysts.

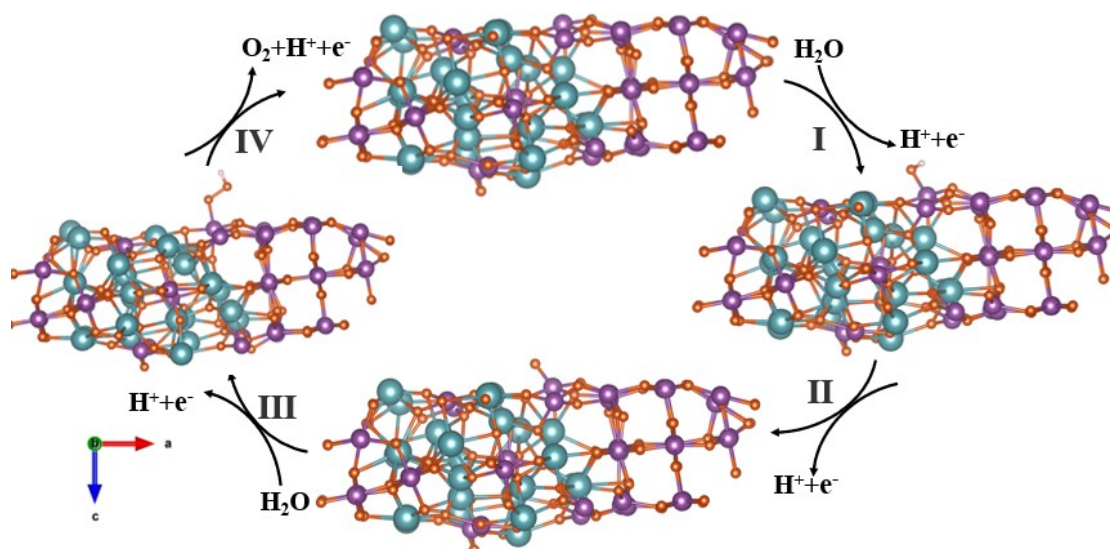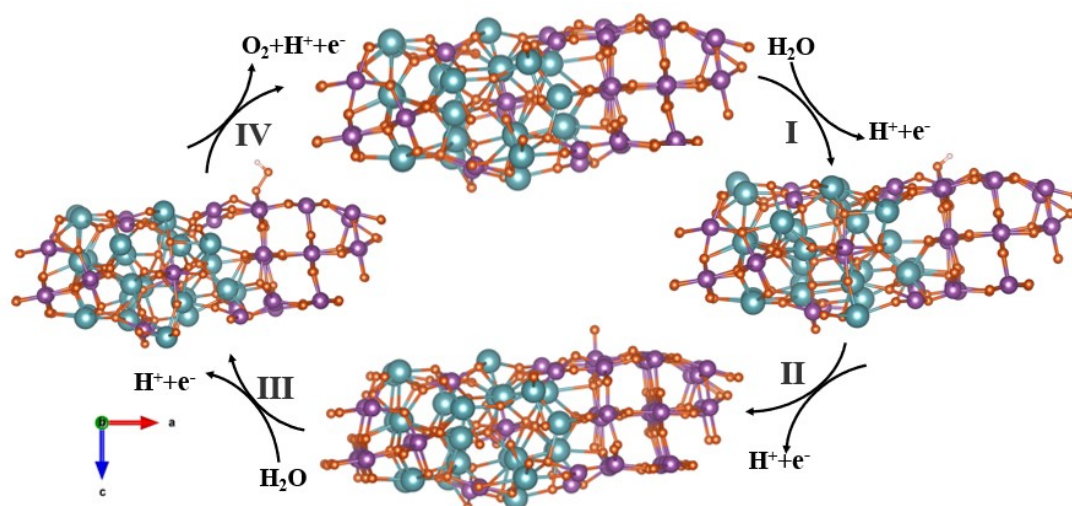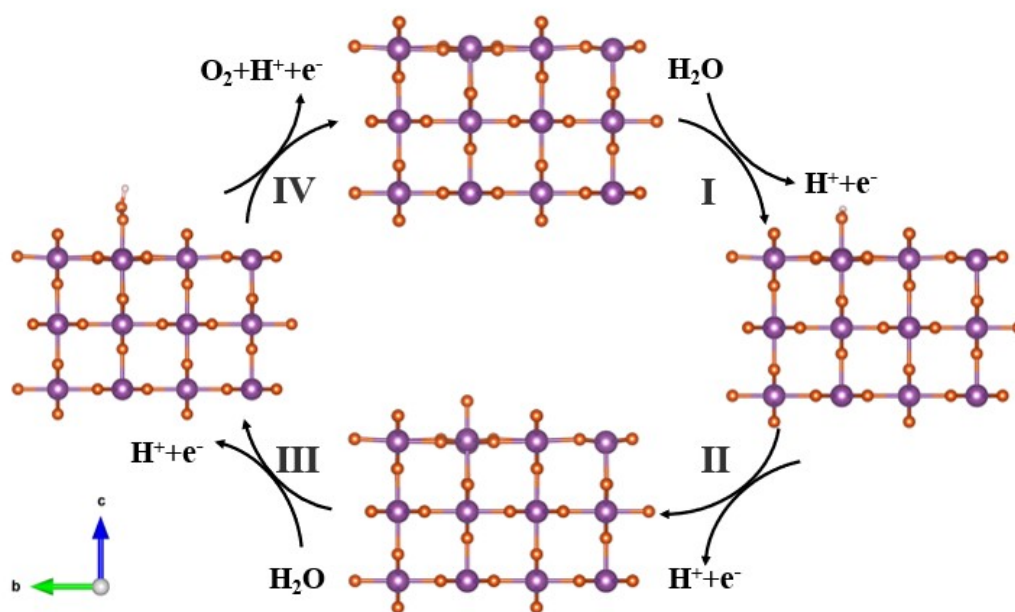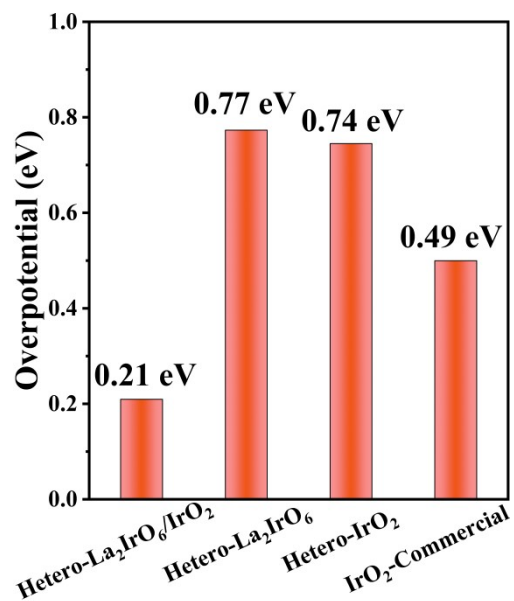**Table S2** Comparison of OER performance of La_2IrO_6/IrO_2 with other recently reported Ir-based electrocatalysts in the acid medium.

Catalysts	Electrolyte	Overpotential (mV) at 10 mA cm^{-2}	Tafel slope (mV dec^{-1})	Ref.
La_2IrO_6/IrO_2	0.5 M H_2SO_4	279	58	this work
IrO_2-C	0.5 M H_2SO_4	322	61	this work
$W_{60}Ir_{20}B_{20}$	0.5 M H_2SO_4	291	78	[10]
Ir_6Ag_9	0.5 M H_2SO_4	285	61	[11]
IrO_2/CNT	0.5 M H_2SO_4	293	67	[12]
P-IrOx@DG	0.5 M H_2SO_4	291	67.5	[13]
Ir/Co_4N	0.5 M H_2SO_4	319	67	[14]
6H-$SrIrO_3$	0.5 M H_2SO_4	292	70.3	[15]
IrCo@NC	0.5 M H_2SO_4	315	101	[16]
Ba_2YIrO_6	0.1 M $HClO_4$	330	67	[17]
$W_{0.57}Ir_{0.43}O_{3-\sigma}$	1 M H_2SO_4	370	125	[18]
Ir-NSG	0.1 M $HClO_4$	265	44.2	[19]
$Ni_{2.53}Ir$	0.5 M H_2SO_4	302	44.6	[20]
IrRu$_x$@Ir	0.5 M H_2SO_4	288	66.2	[21]
BPIr	0.5 M H_2SO_4	290	70	[22]
IrO$_x$/ATO	0.5 M H_2SO_4	360	60	[23]
IrCo	0.5 M H_2SO_4	296.9	68.1	[24]

Note: IrO_2-C: commercial IrO_2; CNT: carbon nanotubes; DG: defective graphene;

NC: nitrogen-doped carbon; NSG: N, S-doped graphene; ATO: antimony-doped

tin oxide

Table S3 EIS parameters of La_2IrO_6/IrO_2 and IrO_2-ES.

	Potential (V vs. SCE)	R_s (ohm)	R_{ct1} (ohm)	CPE_{ct1} (μohm)	R_{ct2} (ohm)	CPE_{ct2} (mohm)	R_{total} (ohm)
La_2IrO_6/IrO_2	1.3	4.73	7.1	19.6	26.3	1.8	39.13
IrO_2-ES	1.3	5.56	8.75	49.2	143	0.97	156.31

Reference

1   W. Gou, M. Zhang, Y. Zou, X. Zhou and Y. Qu, *ChemCatChem*, 2019, **11**, 6008-6014.

2   Y. Jin, W. Huo, L. Zhang, Y. Li, Q. Chen, X. Zhang, S. Yang, H. Nie, X. Zhou and Z. Yang, *Chem. Commun.*, 2021, **57**, 7168-7171.

3   Q. Chen, X. Zhou, X. Zhang, W. Luo, S. Yang, Y. Ge, D. Cai, H. Nie and Z. Yang, *ACS Appl. Mater. Inter.*, 2022, **14**, 20988-20996.

4   X. Zhou, Z. Xia, Z. Tian, Y. Ma and Y. Qu, *J. Mater. Chem. A*, 2015, **3**, 8107-8114.

5   X. Zhou, Z. Xia, Z. Zhang, Y. Ma and Y. Qu, *J. Mater. Chem. A*, 2014, **2**, 11799-11806.

6   P. E. Blöchl, *Phys. Rev. B*, 1994, **50**, 17953-17979.

7   J. P. Perdew, K. Burke and M. Ernzerhof, *Physical Review Letters*, 1996, **77**, 3865-3868.

8   G. Kresse and D. Joubert, *Phys. Rev. B*, 1999, **59**, 1758-1775.

9   H. J. Monkhorst and J. D. Pack, *Phys. Rev. B*, 1976, **13**, 5188-5192.

10   R. Li, H. Wang, F. Hu, K. C. Chan, X. Liu, Z. Lu, J. Wang, Z. Li, L. Zeng, Y. Li, X. Wu and Y. Xiong, *Nat. Commun.*, 2021, **12**, 3540.

11   M. Zhu, Q. Shao, Y. Qian and X. Huang, *Nano Energy*, 2019, **56**, 330-337.

12   J. Guan, D. Li, R. Si, S. Miao, F. Zhang and C. Li, *ACS Catal.*, 2017, **7**, 5983-5986.

13   L. Zhuang, F. Xu, K. Wang, J. Li, C. Liang, W. Zhou, Z. Xu, Z. Shao and Z. Zhu, *Small*, 2021, **17**, 2100121.

14   B. M. Tackett, W. Sheng, S. Kattel, S. Yao, B. Yan, K. A. Kuttiyiel, Q. Wu and J. G. Chen, *ACS Catal.*, 2018, **8**, 2615-2621.

15   L. Yang, G. Yu, X. Ai, W. Yan, H. Duan, W. Chen, X. Li, T. Wang, C. Zhang, X. Huang, J.-S. Chen and X. Zou, *Nat. Commun.*, 2018, **9**, 5236.

16   Y.-Q. Zhou, L. Zhang, H.-L. Suo, W. Hua, S. Indris, Y. Lei, W.-H. Lai, Y.-X. Wang, Z. Hu, H.-K. Liu, S.-L. Chou and S.-X. Dou, *Adv. Funct. Mater.*, 2021, **31**, 2101797.

17   O. Diaz-Morales, S. Raaijman, R. Kortlever, P. J. Kooyman, T. Wezendonk, J. Gascon, W. T. Fu and M. T. M. Koper, *Nat. Commun.*, 2016, **7**, 12363.

18   S. Kumari, B. P. Ajayi, B. Kumar, J. B. Jasinski, M. K. Sunkara and J. M. Spurgeon, *Energy Environ. Sci.*, 2017, **10**, 2432-2440.

19   Q. Wang, C.-Q. Xu, W. Liu, S.-F. Hung, H. Bin Yang, J. Gao, W. Cai, H. M. Chen, J. Li and B. Liu, *Nat. Commun.*, 2020, **11**, 4246.

20   C. Wang, Y. Sui, M. Xu, C. Liu, G. Xiao and B. Zou, *ACS Sustainable Chemistry & Engineering*, 2017, **5**, 9787-9792.

21   Y. Zheng, F. Zhang, G. Wang, D. Lai, L. Zou, Q. Cheng, J. Li, Z. Zou and H. Yang, *J. Power Sources*, 2022, **528**, 231189.

22   J. Mei, T. He, J. Bai, D. Qi, A. Du, T. Liao, G. A. Ayoko, Y. Yamauchi, L. Sun and Z. Sun, *Adv. Mater.*, 2021, **33**, 2104638.

23   H.-S. Oh, H. N. Nong, T. Reier, A. Bergmann, M. Gliech, J. Ferreira de Araújo, E. Willinger, R. Schlögl, D. Teschner and P. Strasser, *J. Am. Chem. Soc.*, 2016,

138, 12552-12563.

24   Y. Zhang, G. Zhang, M. Zhang, X. Zhu, P. Shi, S. Wang and A.-L. Wang, *Chem. Eng. J.*, 2022, **433**, 133577.